ACS OMEGA

http://pubs.acs.org/journal/acsodf

Article

MOF-Derived Long Spindle-like Carbon-Coated Ternary Transition-Metal-Oxide Composite for Lithium Storage

Liming Wu, Yan-gai Liu,* Hang Zhao, Zekun Wang, Bing Zhu, Xi Zhang, Peijie He, Yicen Liu, and Tao Yang*

Cite This: *ACS Omega* 2022, 7, 16837−16846

Read Online

ACCESS | Metrics & More | Article Recommendations | Supporting Information

ABSTRACT: Fe_3O_4 is a promising alternative for next-generation lithium-ion batteries (LIBs). However, its poor cycle stability due to the large volume effect during cycling and poor conductivity hinders its application. Herein, we have successfully designed and prepared a carbon-coated ternary transition-metal-oxide composite (noted as $(FeCoNi)_3O_4$@C), which is derived from FeCoNi-MOF-74 (denoted as FeCoNi-211-24). $(FeCoNi)_3O_4$@C perfectly inherited the long spindle-shaped precursor structure, and $(FeCoNi)_3O_4$ particles grew *in situ* on the precursor surface. The ordered particles and the carbon-coated structure inhibited the agglomeration of particles, improving the material's cycle stability and conductivity. Therefore, the electrode exhibited excellent electrochemical performance. Specifically, $(FeCoNi)_3O_4$@C-700 presented excellent initial discharge capacity (763.1 mAh g^{-1} at 0.2 A g^{-1}), high initial coulombic efficiency (73.8%), excellent rate capability, and cycle stability (634.6 mAh g^{-1} at 0.5 A g^{-1} after 505 cycles). This study provides a novel idea for developing anode materials for LIBs.

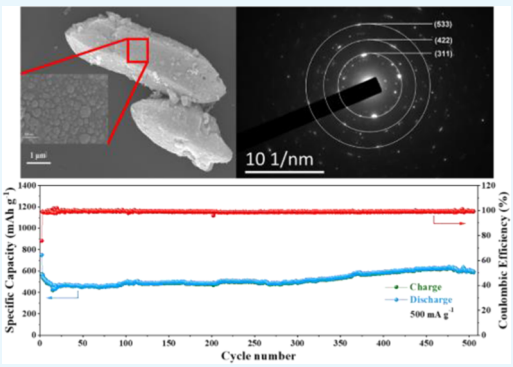

1. INTRODUCTION

Nowadays, rechargeable lithium-ion batteries (LIBs) have become an irreplaceable part of energy storage devices (ESDs) in various fields, such as phones, digital cameras, and personal computers, for their high energy density, high working voltage, fast charge rate, and long cycle life.[1] However, the demand for energy increases rapidly with science and technology development, which requires updating the ESDs. Anode materials are important battery components that determine the performance of batteries. Due to their limited theoretical capacity (372 mAh g^{-1}) and poor performance, current commercial anode graphite gradually can hardly meet the energy demand presently.[2] Transition-metal oxides (TMOs) show higher operating voltages and better safety than graphite-based anode materials. Besides, their various chemical valence states and different morphological characteristics make them promising anode materials for next-generation LIBs.[3]

Among TMOs, Fe_3O_4 especially exhibits a high theoretical specific capacity and is eco-friendly, naturally abundant, and cost-effective.[4] However, the huge volume effect and kinetic constraints result in a poor cycle and rate performance during operation, hindering its application.[5,6] To solve these problems, several studies have been conducted on the following aspects: (1) Preparation of carbon-coated Fe_3O_4 nanoparticles. Ru successfully prepared N-doped carbon-coated Fe_3O_4 composites (Fe_3O_4@NC) by poly(acrylonitrile) (PAN) phase conversion method. The carbon-coated structure can enhance the electron conductivity and buffer the volume change of Fe_3O_4 nanoparticles during cycling.[7] (2) Preparation of Fe_3O_4 nanoparticles with a three-dimensional (3D) porous structure. Wu reported a 3D porous Fe_3O_4 prepared via template-assisted and subsequent electrochemical deposition methods. The porous Fe_3O_4 electrodes show better cyclability and enhanced rate capabilities attributed to improved electrical contact, fast electron transport, and good strain accommodation of the porous electrodes.[8] Nevertheless, the modification improves the cycle and rate performance of Fe_3O_4 finitely because of the serious agglomeration of nanoparticles. Hence, it is needed to design the Fe_3O_4 nanostructure to avoid agglomeration.

A multimetal method was introduced because polymetallic compounds show better electrochemical activity, conductivity, and stability than the corresponding single-metal counterparts when used as electrodes for LIBs.[9] Besides, the volume expansion rate difference between different TMOs can effectively reduce the structural collapse possibility during the cycle. Metal−organic frameworks (MOFs) show apparent advantages of high specific surface area, high porosity, and low density.[10,11] Using MOFs as templates can obtain ternary

Received: March 31, 2022
Accepted: April 26, 2022
Published: May 5, 2022

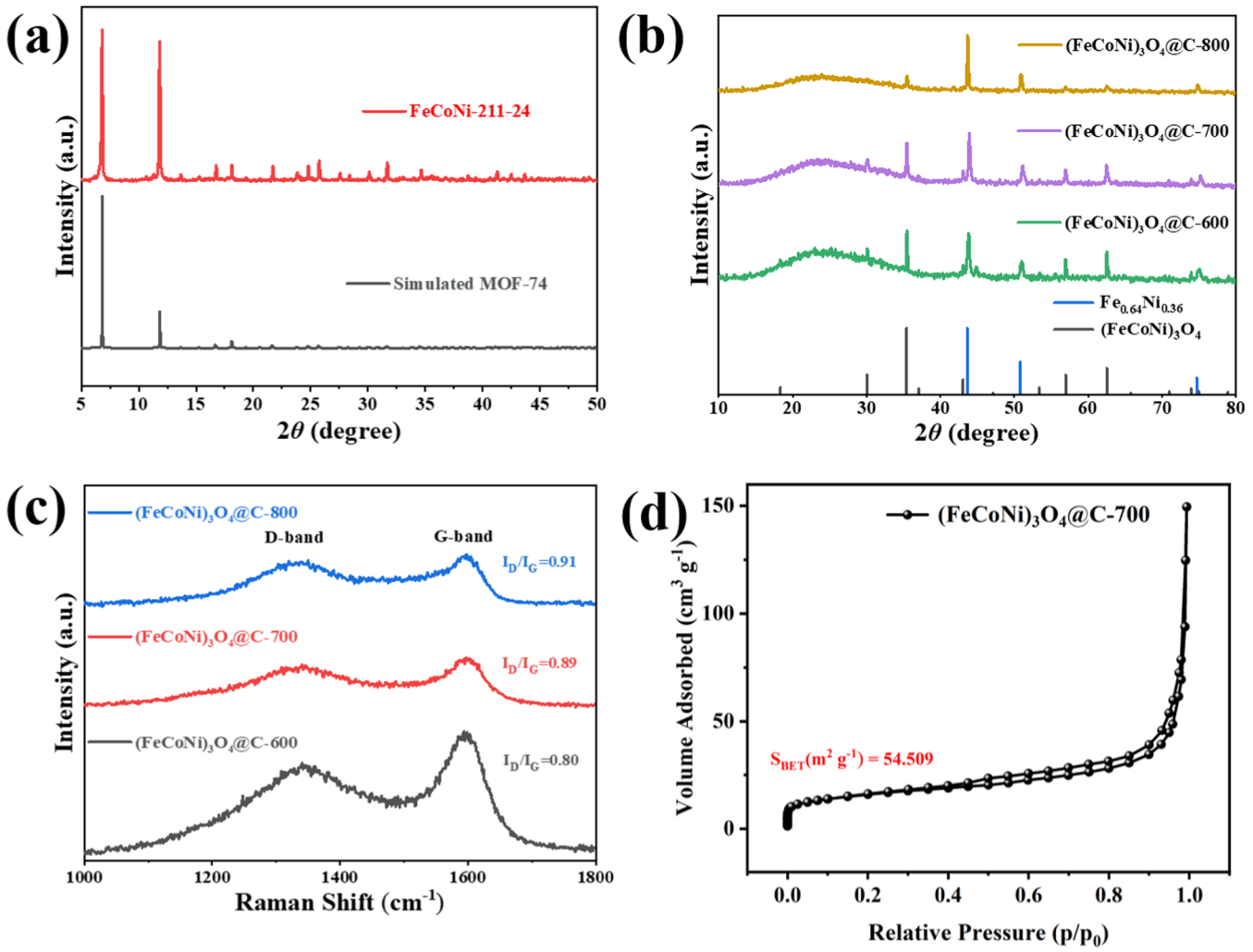

Figure 1. (a) XRD patterns of FeCoNi-211-24 and (b) XRD patterns and (c) Raman spectra of $(FeCoNi)_3O_4$@C-600, 700, and 800. (d) N_2 adsorption/desorption curve of $(FeCoNi)_3O_4$@C-700.

TMOs with uniform element distribution and convert the organic ligands of MOFs into continuous and uniform carbon coated on the TMOs surface, which can effectively alleviate the agglomeration of nanoparticles.

Herein, $(FeCoNi)_3O_4$@C composites were designed and synthesized by a facile one-step pyrolysis method using FeCoNi-211-24 as a template. $(FeCoNi)_3O_4$ single-crystal particles grow *in situ* on the precursor surface, effectively precluding the agglomeration of metal oxides and improving the rate performance. Additionally, the grains and crystal surfaces of $(FeCoNi)_3O_4$ nanoparticles provided a huge specific surface area and several active sites for the material, which is beneficial for improving the material's capacity. Furthermore, the $(FeCoNi)_3O_4$ single-crystal particles connected by carbon formed a polycrystalline long spindle-shaped $(FeCoNi)_3O_4$@C composite. The existence of carbon species bonds in the single-crystal particles inhibits the agglomeration of nanoparticles and improves the cycle stability, conductivity, and ion transport of materials. This work provides a novel idea for TMOs as anode materials for LIBs.

2. EXPERIMENTAL SECTION

2.1. Synthesis of FeCoNi-211-24. The FeCoNi-211-24 crystals were synthesized following a reported method.[12] $Co(NO_3)_2{\cdot}6H_2O$ (0.8384 g), $Ni(NO_3)_2{\cdot}6H_2O$ (0.8376 g), $FeSO_4{\cdot}7H_2O$ (1.6016 g), and 2,5-dihydroxyterephthalic acid (0.72 g) were dissolved in 10 mL of deionized water, and 60 mL of *N*,*N*-dimethylformamide (DMF) and 10 mL of ethanol were successively added to the mixed solution. The mixture was dispersed in a cell grinder for 10 min after mixing and then stirred magnetically for 30 min. Then, the prepared solution was transferred to an autoclave and heated at 120 °C for 24 h. After cooling sufficiently, the products were centrifuged and washed with ethanol and deionized water, and then the products were dried in a vacuum oven at 60 °C for 24 h to obtain FeCoNi-211-24.

2.2. Synthesis of $(FeCoNi)_3O_4$@C. The obtained FeCoNi-211-24 in the first step was placed in a corundum crucible and pyrolyzed in a tubular furnace at 600−900 °C in a nitrogen atmosphere for 2 h. The obtained samples are $(FeCoNi)_3O_4$@C, which were denoted as $(FeCoNi)_3O_4$@C-600, $(FeCoNi)_3O_4$@C-700, $(FeCoNi)_3O_4$@C-800, and $(FeCoNi)_3O_4$@C-900 according to different preparation conditions.

2.3. Material Characterization. X-ray diffraction (XRD, Bruker, D8 Venture) with Cu Kα radiation (λ = 1.5418 Å) was employed to determine the crystallographic phases and phase purity of the products. Field emission scanning electron microscopy (SEM, Gemini-300) and transmission electron

https://doi.org/10.1021/acsomega.2c01988
ACS Omega 2022, 7, 16837−16846

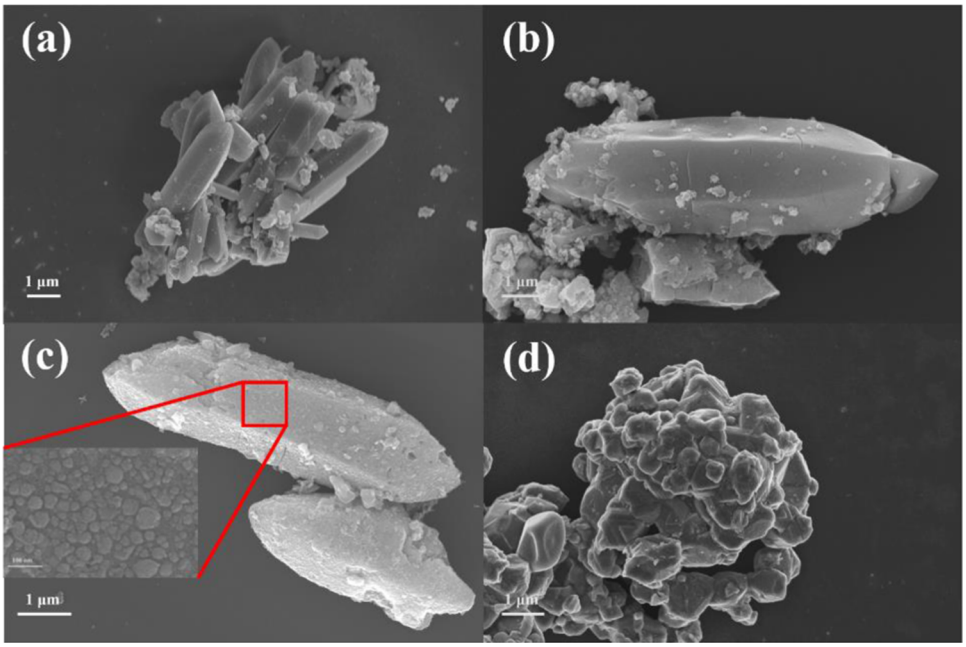

Figure 2. (a) SEM images of FeCoNi-211-24 and (b−d) $(FeCoNi)_3O_4$@C-600, 700, and 800.

microscopy (TEM, JEM-2100F) were applied to characterize the morphology and distribution of samples. X-ray photoelectron spectroscopy (XPS, Scientific K-Alpha) was used to measure the surface chemical states of the products. Raman spectra of anode materials were recorded by a Renishaw (inVia plus) Raman laser microscope. TG-DSC was performed on a NETZSCH (200F3).

2.4. Electrochemical Measurements. The obtained material $(FeCoNi)_3O_4$@C was applied as the anode. The electrochemical measurements were carried out at room temperature using LIR2032 coin-type half cells. The working electrode was prepared by mixing $(FeCoNi)_3O_4$@C, carboxymethylcellulose (CMC), and acetylene black in deionized water with a weight ratio of 8:1:1. The slurry, thoroughly ground in a mortar for 30 min, was coated onto a piece of Cu foil and left to dry at 60 °C under vacuum for 12 h. LIBs were assembled in an Ar-filled glovebox, where water and oxygen concentrations were below 1 ppm. Lithium metal was used as the counter electrode, using a Celgard 2400 membrane as a separator, and 1.1 M LiPF6 in a mixture of ethylene carbonate (EC), dimethyl carbonate (DMC), and vinylene carbonate (VC) (1:1:1 in weight) was used as the electrolyte. Battery test systems (LAND CT2001A) were employed to record the constant current charge and discharge performance of the anode material in the voltage range of 0.01−3.0 V. Electrochemical impedance spectroscopy (EIS) and cyclic voltammetry (CV) curves were tested at 25 °C with the electrochemical workstation (CHI604E) in the voltage range of 0.01−3 V.

3. RESULTS AND DISCUSSION

Based on the literature[12−14] and combined with the XRD diffraction pattern of FeCoNi-MOF-74 (Figures 1a, S1, and S2), FeCoNi-211-24 was successfully prepared by a simple hydrothermal method in this study. However, MOFs are seldomly used as electrode materials due to their poor conductivity and cycle stability. Using MOFs as templates or precursors, carbon-coated metal oxides with high porosity can be obtained by controlled pyrolysis reaction.[15] Therefore, $(FeCoNi)_3O_4$@C with a long spindle shape, which is electrochemically active and has high conductivity and cycle stability, was synthesized by pyrolyzing FeCoNi-211-24 in an N_2 atmosphere at different temperatures.

Figure 1b shows the phase transition of FeCoNi-211-24 during pyrolysis in a N_2 atmosphere. Obviously, the products obtained at different pyrolysis temperatures display a wide peak at 2θ = 22.9°, indicating amorphous carbon formation.[5] The diffraction peaks at 30.1, 35.4, 56.6, and 62.5° correspond to the (220), (311), (333), and (440) planes of $(FeCoNi)_3O_4$ phase. The proportion of alloy phases in the product increases continuously as the temperature increases. At 800 °C, the alloy phase replaced $(FeCoNi)_3O_4$ became the main product component, and the metal oxide phase completely transformed into the alloy phase at 900 °C (Figure S3).

Electronic conductivity and ion transport properties significantly influence the electrochemical properties. The existence of carbon on the anode surface can effectively improve these properties.[7,16] Therefore, Raman spectroscopy was applied to evaluate the $(FeCoNi)_3O_4$@C sample characteristics (Figure 1c). The two distinct characteristic diffraction peaks near 1300 and 1580 cm^{-1} are the D band and G band, respectively. The D band measures the C lattice defects, and the G band represents the in-plane stretching vibration of the C sp^2 hybridization.[17] The intensity ratio between the D and G bands reflects the surface defects and lattice distortion of the as-prepared samples, indicating the disordered carbon nature.[18] Figure 1c shows that the I_D/I_G ratios of the samples are 0.80, 0.89, and 0.91, respectively. These values increase continuously as temperature increases, indicating that the surface defects of $(FeCoNi)_3O_4$@C increase continuously. Note that when the pyrolysis temperature increases by 100 °C, the I_D/I_G value of $(FeCoNi)_3O_4$@C-700 increases greatly compared to that of $(FeCoNi)_3O_4$@C-600. However, the I_D/I_G value of $(FeCoNi)_3O_4$@C-800 increased slightly, indicating that the temperature increment contributes slightly to the increment in surface defects at 700 °C. The high I_D/I_G value provides many surface defects and

https://doi.org/10.1021/acsomega.2c01988
ACS Omega 2022, 7, 16837−16846

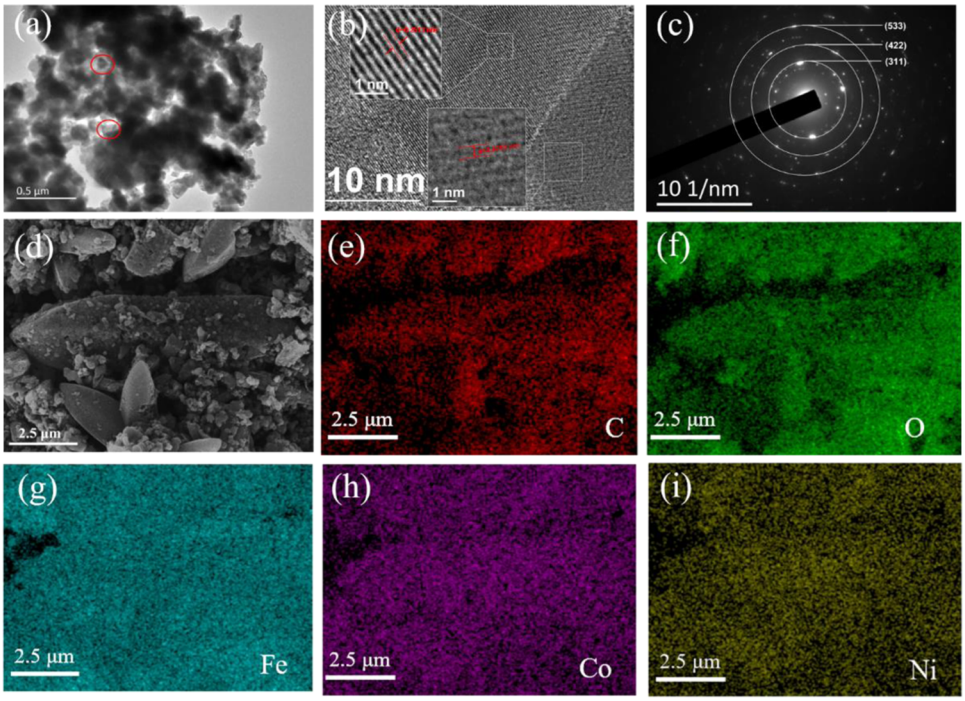

Figure 3. (a) TEM image, (b) HR-TEM image, (c) selected area electron diffraction (SAED) pattern , and (d–i) the corresponding elemental mapping distribution of $(FeCoNi)_3O_4$@C-700.

ion storage active sites, which enhance the specific capacity of the materials.[19] Therefore, it can be speculated reasonably that $(FeCoNi)_3O_4$@C-700 has better electrochemical performance.

N_2 adsorption and desorption isotherms measurement was utilized to study the specific surface area and the porous properties of as-synthesized samples. As shown in Figure 1d, the specific surface area of $(FeCoNi)_3O_4$@C-700 (54.509 $m^2 g^{-1}$) is larger than that of $(FeCoNi)_3O_4$@C-800 (10.381 $m^2 g^{-1}$) (Figure S4). The larger specific surface area means that more active sites are exposed and the contact area between electrolyte and material increases, which greatly improves the electrochemical performance.

Figure 2 shows the SEM images of the FeCoNi-211-24 precursor and $(FeCoNi)_3O_4$@C samples prepared at different temperatures. Figure 2a shows a long spindle shape corresponding to the precursor. During pyrolysis, cracks gradually appear on the surface of the long spindle precursor (Figure 2b) as the temperature increases continuously, and irregular octahedral $(FeCoNi)_3O_4$ crystals (Figure S5) grow *in situ* on the surface. The sample obtained at 700 °C perfectly inherits the unique spindle precursor structure (Figure 2c) and exposes more $(FeCoNi)_3O_4$ grains and crystal planes on the surface; $(FeCoNi)_3O_4$ single-crystal nanoparticles connected by the surface carbon formed a long spindle polycrystalline composite $(FeCoNi)_3O_4$@C. As the temperature increases, the alloying degree of the $(FeCoNi)_3O_4$ continually increases, along with the structural collapse of the precursor. The $(FeCoNi)_3O_4$@C-800 sample agglomerated to form a huge polycrystalline particle with a particle size of several microns (Figure 2d).

The TEM image (Figure 3a) confirms that $(FeCoNi)_3O_4$@C-700 comprises carbon-coated irregular octahedral nanoparticles (red circle), where the amorphous carbon layer thickness is 3–5 nm (Figure S6). Due to the different atomic radii of Fe, Co, and Ni, the molar ratio content affects the sample's lattice parameters.[12,20] The high-resolution TEM image (Figure 3b) shows lattice fringes' pitches of 0.4703 and 0.2513 nm corresponding to the $(FeCoNi)_3O_4$@C(111) and (311) planes. Additionally, several clear electron diffraction rings of $(FeCoNi)_3O_4$@C-700 shown in the selected area electron diffraction image (Figure 3c) indicate that the as-prepared sample is a polycrystalline material comprising single-crystal particles. The well-defined diffraction rings correspond to the (311), (422), and (533) crystal planes of $(FeCoNi)_3O_4$. The mapping image of the energy-dispersive system (Figure 3d–i) shows that Fe, Co, Ni, O, and C are evenly distributed in samples.

To further understand the chemical state and composition of the samples, the electronic structure and elemental valence states of $(FeCoNi)_3O_4$@C-700 were analyzed using X-ray photoelectron spectroscopy. The spectrum (Figure 4a) confirms the presence of Fe, Co, Ni, C, and O in the sample. The peak at 284.77 eV of the C 1s high-resolution XPS spectrum (Figure 4b) corresponds to the C–C bond, confirming the presence of amorphous carbon. The peaks at 285.79 and 288.98 eV are attributed to C–O and O–C=O.[10,21] The peak at 530.10 eV of the O 1s spectrum corresponds to (FeCoNi)–O. The binding energies at 531.92 and 533.82 eV are the bonds between carbon- and oxygen-containing groups on the surface of metal oxides, which are C–O, and –O–C=O (Figure 4c).[10] Figure 4d shows the Fe state; the Fe 2p spectrum can be decomposed into five peaks. The peaks at 710.41 and 723.93 eV reveal Fe^{2+} existence. The peak at 718.31 eV is attributed to the satellite, which relates to the oscillatory excitation of high spin Fe^{2+}, whereas the peaks located at 712.45 and 726.24 eV correspond to Fe^{3+}.[22,23] For the Co 2p spectrum (Figure 4e), the peaks at 781.41 and 796.76 eV are attributed to the Co $2p_{3/2}$ and Co $2p_{1/2}$ electrons of Co^{2+}, whereas the satellite peaks are observed at 785.26 and 802.63 eV. Additionally, the peaks

https://doi.org/10.1021/acsomega.2c01988
ACS Omega 2022, 7, 16837–16846

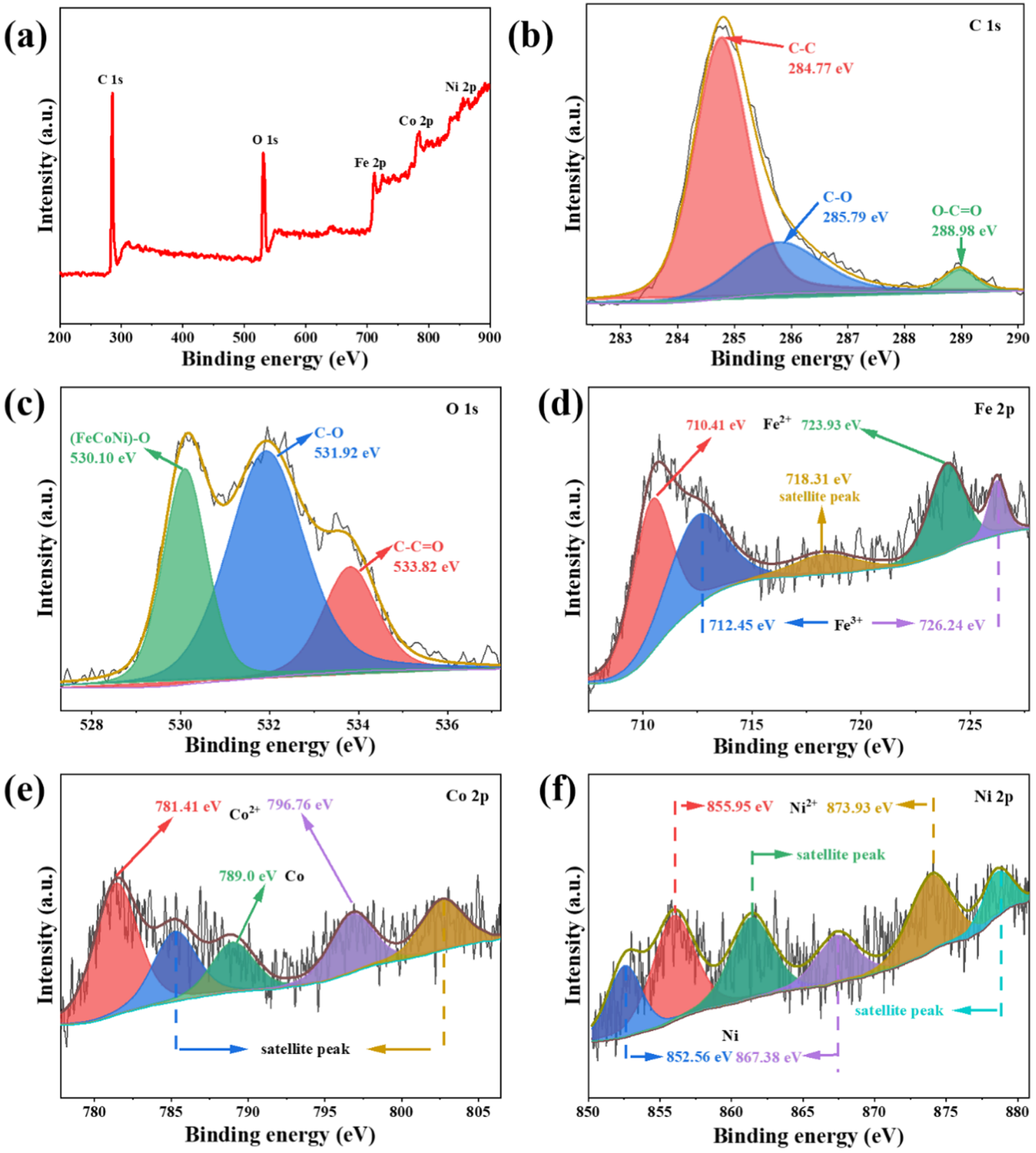

Figure 4. (a) XPS spectra, (b) C 1s spectrum, (c) O 1s spectrum, (d) Fe 2p spectrum, (e) Co 2p spectrum, and (f) Ni 2p spectrum of $(FeCoNi)_3O_4$@C-700.

detected at 789.0 eV correspond to the status of metallic Co.[24] Three unique Ni statuses can be observed by deconvoluting the Ni 2p spectrum (Figure 4f), which are Ni, Ni^{2+}, and satellites. The two distinct peaks at 852.56 and 867.38 eV correspond to metallic Ni, where the binding energies at 855.95 and 873.93 eV relate to Ni $2p_{3/2}$ and Ni $2p_{1/2}$ electrons, respectively.[12,25] Compared with the pure metallic Fe, Ni, and Co species, the binding energy of the three metal elements drifted positively, indicating better conductivity.[13,26]

Furthermore, the electrochemical performance of $(FeCoNi)_3O_4$@C was evaluated as an anode material for LIBs (Figure 5). Figure 5a shows the CV curves of $(FeCoNi)_3O_4$@C-700 at 0.1 mV s^{-1}. During the initial lithiation, three reduction peaks are observed at 0.96, 0.52, and 0.01 V, respectively. The reduction peak at 0.96 V is attributed to the

https://doi.org/10.1021/acsomega.2c01988
ACS Omega 2022, 7, 16837−16846

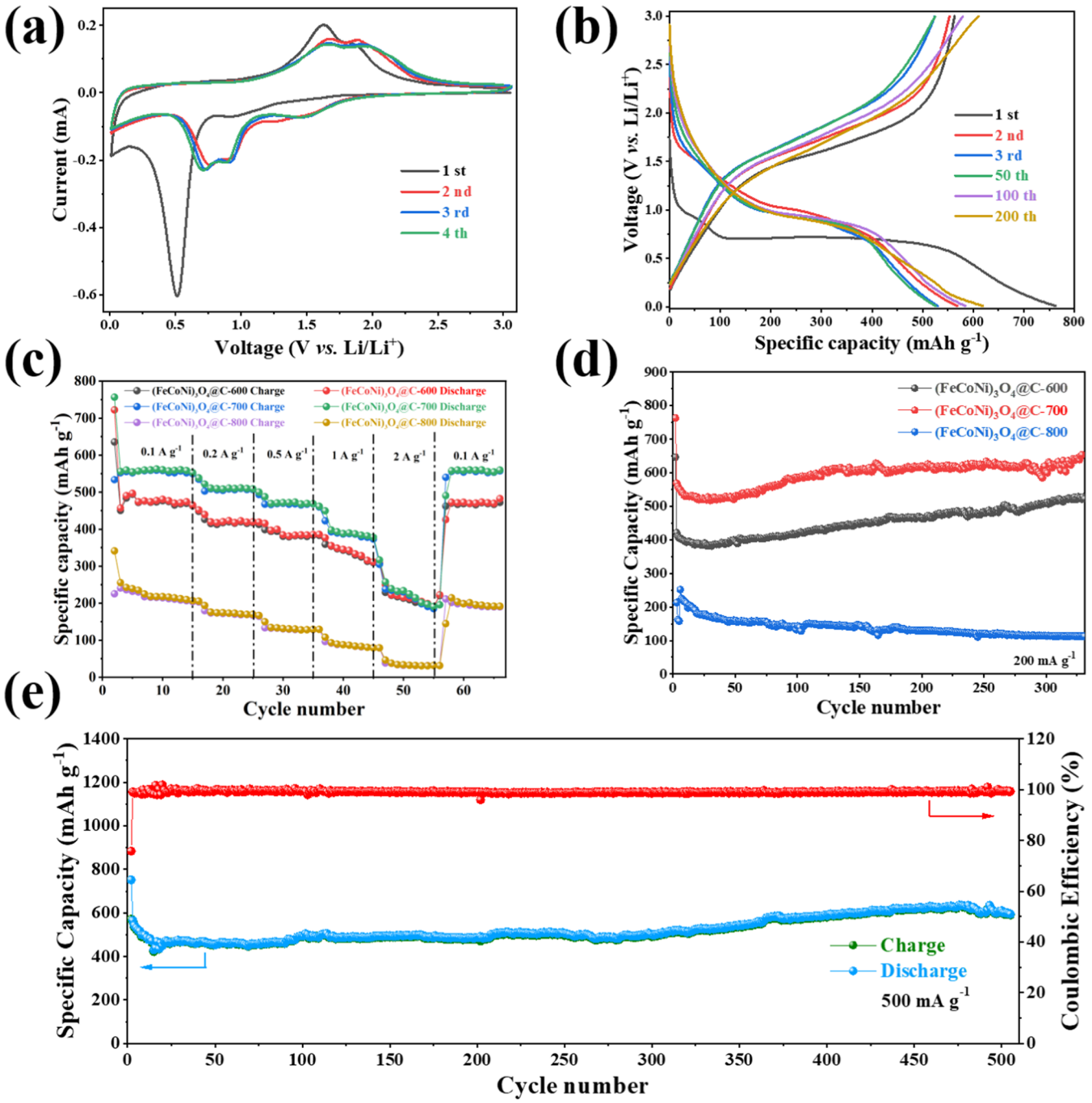

Figure 5. (a) CV curves at a scan rate of 0.1 mV s^{-1}; (b) galvanostatic discharge−charge curves at a current density of 200 mA g^{-1} of $(FeCoNi)_3O_4$@C-700; (c) rate performance of sample $(FeCoNi)_3O_4$@C-600, 700, and 800 at different current densities from 0.1 to 2 A g^{-1}; (d) comparison of cycle performance of samples $(FeCoNi)_3O_4$@C-600, 700, and 800 at a current density of 200 mA g^{-1}; and (e) cycling performance and coulombic efficiency of sample $(FeCoNi)_3O_4$@C-700 at 500 mA g^{-1}.

inserting reaction, which produces $Li_x[(FeCoNi)_3O_4]$.[5,21] The reduction peak at 0.52 V relates to two factors. Owing to the conversion reaction, the $(FeCoNi)_3O_4$ phase transforms into the $(FeCoNi)^0$ phase; however, the peak is related to the electrolyte decomposition, which forms the solid electrolyte interface (SEI) layer. The peak near 0.01 V relates to Li^+ intercalation into the amorphous porous carbon, causing the carbon matrix lithiation.[17,27] During the first anode cycle, two oxidation peaks were detected at 1.6 and 1.8 V, corresponding to the reversible oxidation of $(FeCoNi)^0$ to $(FeCoNi)_3O_4$. Subsequently, the CV cycle curves and peak locations of the sample almost overlap, indicating good cycle stability and reversibility. The reduction peak at 1.5 V corresponds to the material's deinserting reaction, whereas peaks at 0.91 and 0.73 V are attributed to the $(FeCoNi)_3O_4$ to $(FeCoNi)^0$ reduction reaction. The cyclic process is similar to those in the literature.[8,10,28] Note that the reduction peak at 0.52 V disappears in the first cycle, indicating the formation of the stable SEI film on the material's surface, which enhances the rate performance and cycle stability of the material.[17] The reactions involved in the circulation process are as follows

https://doi.org/10.1021/acsomega.2c01988
ACS Omega 2022, 7, 16837−16846

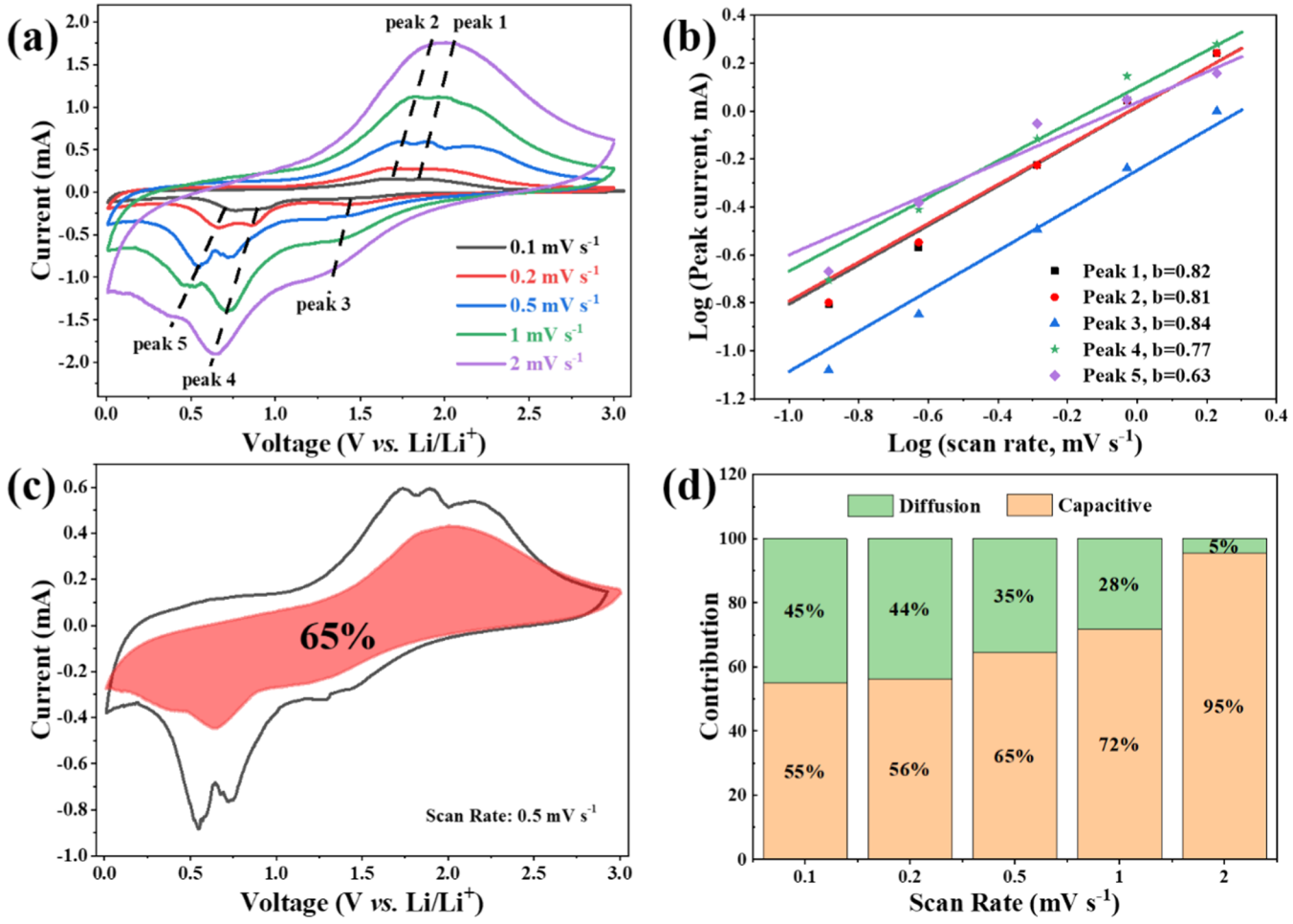

Figure 6. Electrochemical kinetic analysis of the $(FeCoNi)_3O_4$@C-700 electrode. (a) CV curves at different scan rates from 0.1 to 2 mV s^{-1}; (b) *b* value calculated by log(peak current) *vs* log(scan rate); (c) diffusion contribution and capacitance contribution at 0.5 mV s^{-1}; and (d) comparison of diffusion contribution and capacitance contribution at various scan rates.

$$(FeCoNi)_3O_4 + xLi^+ \rightarrow Li_x[(FeCoNi)_3O_4] \quad (1)$$

$$Li_x[(FeCoNi)_3O_4] + Li^+ \rightarrow (FeCoNi)^0 + Li_2O \quad (2)$$

$$(FeCoNi)^0 + Li_2O \rightarrow (FeCoNi)_3O_4 + Li^+ \quad (3)$$

Figure 5b exhibits the $(FeCoNi)_3O_4$@C-700 galvanostatic charge−discharge (GCD) curves of the 1st, 2nd, 3rd, 50th, 100th, and 200th cycles at a current density of 200 mA g^{-1}. $(FeCoNi)_3O_4$@C-700 presents initial discharge and charge-specific capacities of 763.1 and 563.4 mAh g^{-1}, respectively, with an initial coulombic efficiency (ICE) of 73.8%. The ICE values of $(FeCoNi)_3O_4$@C-600 and $(FeCoNi)_3O_4$@C-800 are 63.3 and 65.2%, respectively (Figure S7). The irreversible capacity in the first cycle was caused by the formation of SEI film and electrolyte decomposition.[17,23,29] A discharge platform can be observed at ∼0.9 V, and an ultralong plateau appears at ∼0.7 V in the first cycle. Discharge voltage plateaus located at ∼1.6 and 1.0 V and a charge voltage platform at ∼1.7 V can be observed in the subsequent cycle, corresponding to the redox in the process. The GCD results are consistent with the CV data. Moreover, from the second cycle, the coulombic efficiency (CE) of $(FeCoNi)_3O_4$@C-700 recovered to 97.36%, indicating the sample's excellent cycle reversibility.

The rate performance of $(FeCoNi)_3O_4$@C-600, $(FeCoNi)_3O_4$@C-700, and $(FeCoNi)_3O_4$@C-800 was measured at current densities of 0.1, 0.2, 0.5, 1, 2, and 0.1 A g^{-1} (Figure 5c). The reversible specific capacities of $(FeCoNi)_3O_4$@C-700 are 572.5, 512.4, 471.1, and 386.6 mAh g^{-1}, corresponding to 0.1−1 A g^{-1}. Impressively, the reversible specific capacities of $(FeCoNi)_3O_4$@C-700 remained at 558.3 mAh g^{-1} when the current density dropped to 0.1 A g^{-1}, indicating the excellent reversibility of $(FeCoNi)_3O_4$@C-700. Surprisingly, $(FeCoNi)_3O_4$@C-800 shows reversible capacities of ∼280 mAh g^{-1} (Figure S8); when it was exposed at a high current density of 2 A g^{-1} for 800 cycles, the CE value is close to 100%, indicating its excellent cycle stability at high current density.

Furthermore, the lithium storage stability of the electrode was investigated at 200 mA g^{-1} (Figure 5d). The initial discharge specific capacity of $(FeCoNi)_3O_4$@C-700 is 763.1 mAh g^{-1} because of the distinct structural and morphological reconstructions, which caused a large volume change, resulting in a decreased capacity in the first 30 cycles. However, the reconstruction provides new active sites and surfaces, indicating that the surface reactions occur even with higher kinetics, leading to continuous capacity increment in the subsequent cycle.[17,21,23] After 330 cycles, the reversible specific capacity and CE of $(FeCoNi)_3O_4$@C-700 are ∼653.4 mAh g^{-1} and 100%, respectively. Under the same conditions, the after-cycling reversible specific capacities of $(FeCoNi)_3O_4$@C-600 and $(FeCoNi)_3O_4$@C-800 are 527.8 and 120.6 mAh g^{-1}, respectively. According to Figure 2d, the structure of

https://doi.org/10.1021/acsomega.2c01988
ACS Omega 2022, 7, 16837−16846

$(FeCoNi)_3O_4$@C-800 was collapsed, which seriously affected its electrochemical performance. However, $(FeCoNi)_3O_4$@C-700 maintained the long spindle-shaped structure with more $(FeCoNi)_3O_4$ transition-metal-oxide crystal particles formed on its surface. The active sites were increased, resulting in a large increase in electrochemical performance. To prove the excellent electrochemical performance of $(FeCoNi)_3O_4$@C-700, the long-cycling performance was investigated at a high current density of 0.5 A g^{-1}. Figure 5e shows that the specific discharge capacity of $(FeCoNi)_3O_4$@C-700 is 634.6 mAh g^{-1} after 505 cycles (CE is 99.22%). The $(FeCoNi)_3O_4$@C-700 sample comprises single-crystal particles with controlled shapes and particle sizes, perfectly inherits the skeleton structure of the precursor FeCoNi-211-24, and forms a unique long spindle-shaped carbon shell-coating structure, showing high capacity and excellent cycle stability. Therefore, the impressive long-cycling stability of the $(FeCoNi)_3O_4$@C-700 electrode is attributed to the unique carbon shell structure, which accelerates electron conduction and effectively inhibits the electrode volume expansion in the cycle process.[19,29,30]

Figure S9 shows the electrochemical impedance spectra (EIS) of $(FeCoNi)_3O_4$@C-600 and $(FeCoNi)_3O_4$@C-700. The high- and medium-frequency semicircles are attributed to the contact and charge transfer impedances, respectively. The inclined straight line is associated with Warburg impedance corresponding to the lithium-diffusion process. The diameters of the high-frequency and intermediate-frequency semicircles produced by $(FeCoNi)_3O_4$@C-700 are smaller than that of $(FeCoNi)_3O_4$@C-600, indicating that $(FeCoNi)_3O_4$@C-700 has better conductivity and ionic conductivity.

Additionally, the $(FeCoNi)_3O_4$@C-700 electrode was tested at different sweep rates of 0.1−2.0 mV s^{-1} in the potential range of 0.01−3.00 V to explore the electrode electrochemical kinetics. The CV curves at different scanning rates (Figure 6a) show similar shapes. According to previous studies, electrochemical storage behavior can be subdivided into faradic (charge transfer) and nonfaradic (pseudo-capacitive behavior) processes. The peak current (i) and scanning rate (v) are utilized to study pseudo-capacitance by the following formulas[17−19]

$$i = av^b \tag{4}$$

$$\log(i) = b\log(\nu) + \log(a) \tag{5}$$

Generally, the process is diffusion-controlled when the adjustable parameter (b) is close to 0.5, but pseudo-capacitance-controlled when b approaches unity. Figure 6b shows the relationship between log(i) and log(ν). Through simulation and calculation, the b values corresponding to the five peaks are 0.82, 0.81, 0.84, 0.77, and 0.63, indicating that the lithium storage behavior of $(FeCoNi)_3O_4$@C-700 is mainly pseudo-capacitance-controlled.

According to the equation describing the relationship between capacitance and diffusion contributions ($i(v) = k_1\nu + k_2\nu^{1/2}$),[17,31] the capacitance contribution of $(FeCoNi)_3O_4$@C-700 is 64.52% at a scanning rate of 0.5 mV s^{-1} (Figure 6c). Figure 6d shows that the capacitance contribution rate increases as the scanning rate increases. When the scanning speeds are 0.1 and 2 mv s^{-1}, the capacitance contribution rates are 55 and 95%, respectively. Thus, the capacitance behavior in the electrode is closely related to electrochemical kinetics. A high-capacitance contribution rate indicates the rapid transfer of Li^+, reflecting an excellent rate performance.[17,19,32]

4. CONCLUSIONS

Herein, a long spindle-like $(FeCoNi)_3O_4$@C composite was designed and synthesized by a facile one-step high-temperature pyrolysis method using the FeCoNi-211-24 template, which was fabricated by a simple hydrothermal method. The $(FeCoNi)_3O_4$@C-700 sample inherits the long spindle structure of FeCoNi-211-24. The $(FeCoNi)_3O_4$ particles grown *in situ* on the precursor surface and connected by amorphous carbon formed a long polycrystalline spindle $(FeCoNi)_3O_4$@C composite. The structure exposed grains and crystal planes to preclude the agglomeration of metal oxides and provide an enormous specific surface area and several active sites for the material, effectively improving the electrochemical performance of the material. The carbon layer in the material enhances bonding and can effectively improve the material's conductivity and ion transport. The anode shows excellent initial discharge capacity (763.1 mAh g^{-1} at 0.2 A g^{-1}), a high ICE of 73.8%, rate capability, and cycle stability (634.6 mAh g^{-1} at 0.5 A g^{-1} after 505 cycles). By designing and preparing $(FeCoNi)_3O_4$@C as the anode material of LIBs, excellent electrode electrochemical properties are observed.

■ ASSOCIATED CONTENT

Supporting Information

The Supporting Information is available free of charge at https://pubs.acs.org/doi/10.1021/acsomega.2c01988.

Characterization of materials, SEM, TEM, N_2 adsorption/desorption isotherms, and electrochemical properties (PDF)

■ AUTHOR INFORMATION

Corresponding Authors

Yan-gai Liu − *School of Materials Science and Technology, Beijing Key Laboratory of Materials, Utilization of Nonmetallic Minerals and Solid Wastes, National Laboratory of Mineral Materials, China University of Geosciences, Beijing 100083, People's Republic of China*; orcid.org/0000-0002-8148-1699; Email: liuyang@cugb.edu.cn

Tao Yang − *College of Materials & Environmental Engineering, Hangzhou Dianzi University, Hangzhou 310018, People's Republic of China*; orcid.org/0000-0002-6948-0028; Email: yangtao@hdu.edu.cn

Authors

Liming Wu − *School of Materials Science and Technology, Beijing Key Laboratory of Materials, Utilization of Nonmetallic Minerals and Solid Wastes, National Laboratory of Mineral Materials, China University of Geosciences, Beijing 100083, People's Republic of China*

Hang Zhao − *School of Materials Science and Technology, Beijing Key Laboratory of Materials, Utilization of Nonmetallic Minerals and Solid Wastes, National Laboratory of Mineral Materials, China University of Geosciences, Beijing 100083, People's Republic of China*

Zekun Wang − *School of Materials Science and Technology, Beijing Key Laboratory of Materials, Utilization of Nonmetallic Minerals and Solid Wastes, National Laboratory of Mineral Materials, China University of Geosciences, Beijing 100083, People's Republic of China*

Bing Zhu − *School of Materials Science and Technology, Beijing Key Laboratory of Materials, Utilization of Nonmetallic Minerals and Solid Wastes, National Laboratory*

https://doi.org/10.1021/acsomega.2c01988
ACS Omega 2022, 7, 16837−16846

of Mineral Materials, China University of Geosciences, Beijing 100083, People's Republic of China

Xi Zhang − *School of Materials Science and Technology, Beijing Key Laboratory of Materials, Utilization of Nonmetallic Minerals and Solid Wastes, National Laboratory of Mineral Materials, China University of Geosciences, Beijing 100083, People's Republic of China*

Peijie He − *School of Materials Science and Technology, Beijing Key Laboratory of Materials, Utilization of Nonmetallic Minerals and Solid Wastes, National Laboratory of Mineral Materials, China University of Geosciences, Beijing 100083, People's Republic of China*

Yicen Liu − *School of Materials Science and Technology, Beijing Key Laboratory of Materials, Utilization of Nonmetallic Minerals and Solid Wastes, National Laboratory of Mineral Materials, China University of Geosciences, Beijing 100083, People's Republic of China*

Complete contact information is available at: https://pubs.acs.org/10.1021/acsomega.2c01988

Author Contributions

L.W. contributed to conceptualization, methodology, software, and writing—original draft. H.Z., Z.W., and B.Z. performed investigation and formal analysis. X.Z. carried out Data curation. P.H. and Y.L. conducted investigation. Y.-G.L., T.Y. contributed to supervision, funding acquisition, and writing—review and editing.

Notes

The authors declare no competing financial interest.

■ ACKNOWLEDGMENTS

This work was financially supported by the National Natural Science Foundation of China (grant nos. 51772278, 52072348, and 52002101) and the Natural Science Foundation of Zhejiang Province (no. LQ20E020006).

■ REFERENCES

(1) (a) Hartmann, F.; Etter, M.; Cibin, G.; Liers, L.; Terraschke, H.; Bensch, W. Superior Sodium Storage Properties in the Anode Material $NiCr_2S_4$ for Sodium-Ion Batteries: An X-ray Diffraction, Pair Distribution Function, and X-ray Absorption Study Reveals a Conversion Mechanism via Nickel Extrusion. *Adv. Mater.* **2021**, *33*, No. 2101576. (b) Tarascon, J. M.; Armand, M. Issues and challenges facing rechargeable lithium batteries. *Nature* **2001**, *414*, 359−367.

(2) (a) Wu, F.; Maier, J.; Yu, Y. Guidelines and trends for next-generation rechargeable lithium and lithium-ion batteries. *Chem. Soc. Rev.* **2020**, *49*, 1569−1614. (b) Guo, W. X.; Sun, W. W.; Lv, L. P.; Kong, S. F.; Wang, Y. Microwave-Assisted Morphology Evolution of Fe-Based Metal-Organic Frameworks and Their Derived Fe_2O_3 Nanostructures for Li-Ion Storage. *ACS Nano* **2017**, *11*, 4198−4205.

(3) (a) Zheng, M.; Tang, H.; Li, L.; Hu, Q.; Zhang, L.; Xue, H.; Pang, H. Hierarchically Nanostructured Transition Metal Oxides for Lithium-Ion Batteries. *Adv. Sci.* **2018**, *5*, No. 1700592. (b) Poizot, P.; Laruelle, S.; Grugeon, S.; Dupont, L.; Tarascon, J. M. Nano-sized transition-metaloxides as negative-electrode materials for lithium-ion batteries. *Nature* **2000**, *407*, 496−499. (c) Zhao, Y.; Li, X. F.; Yan, B.; Xiong, D. B.; Li, D. J.; Lawes, S.; Sun, X. L. Recent Developments and Understanding of Novel Mixed Transition-Metal Oxides as Anodes in Lithium Ion Batteries. *Adv. Energy Mater.* **2016**, *6*, No. 1502175.

(4) (a) Xu, D.; Ma, K.; Chen, L.; Hu, Y. J.; Jiang, H.; Li, C. Z. MXene interlayer anchored Fe_3O_4 nanocrystals for ultrafast Li-ion batteries. *Chem. Eng. Sci.* **2020**, *212*, No. 115342. (b) Cao, Z. J.; Ma, X. B. Encapsulated Fe_3O_4 into tubular mesoporous carbon as a superior performance anode material for lithium-ion batteries. *J. Alloys Compd.* **2020**, *815*, No. 152542. (c) Liu, J.; Xu, X. J.; Hu, R. Z.; Yang, L. C.; Zhu, M. Uniform Hierarchical Fe_3O_4@Polypyrrole Nanocages for Superior Lithium Ion Battery Anodes. *Adv. Energy Mater.* **2016**, *6*, No. 1600256.

(5) Zeng, Z.; Zhao, H.; Wang, J.; Lv, P.; Zhang, T.; Xia, Q. Nanostructured Fe_3O_4@C as anode material for lithium-ion batteries. *J. Power Sources* **2014**, *248*, 15−21.

(6) Taberna, P. L.; Mitra, S.; Poizot, P.; Simon, P.; Tarascon, J. M. High rate capabilities Fe_3O_4-based Cu nano-architectured electrodes for lithium-ion battery applications. *Nat. Mater.* **2006**, *5*, 567−573.

(7) Ru, S.; Wang, X.; Ma, G. Q.; Tan, J. Y.; Xiao, H. H.; Ai, Z. Q. Phase inversion synthesis of Fe_3O_4@NC composites with superior lithium. *J. Alloys Compd.* **2020**, *844*, No. 156039.

(8) Wu, H.; Du, N.; Wang, J. Z.; Zhang, H.; Yang, D. R. Three-dimensionally porous Fe_3O_4 as high-performance anode materials for lithium-ion batteries. *J. Power Sources* **2014**, *246*, 198−203.

(9) (a) Dai, S.; Bai, Y.; Shen, W.; Zhang, S.; Hu, H.; Fu, J.; Wang, X.; Hu, C.; Liu, M. Core-shell structured Fe_2O_3@Fe_3C@C nanochains and Ni-Co carbonate hydroxide hybridized microspheres for high-performance battery-type supercapacitor. *J. Power Sources* **2021**, *482*, No. 228915. (b) Kakarla, A. K.; Narsimulu, D.; Yu, J. S. Two-dimensional porous $NiCo_2O_4$ nanostructures for use as advanced high-performance anode material in lithium-ion batteries. *J. Alloys Compd.* **2021**, *886*, No. 161224.

(10) Li, Z.; Hu, X.; Li, B.; Wang, X.; Shi, Z.; Lu, J.; Wang, Z. MOF-derived Fe_3O_4 hierarchical nanocomposites encapsulated by carbon shells as high-performance anodes for Li-storage systems. *J. Alloys Compd.* **2021**, *875*, No. 159906.

(11) Wang, L.; Han, Y. Z.; Feng, X.; Zhou, J. W.; Qi, P. F.; Wang, B. Metal-organic frameworks for energy storage: Batteries and supercapacitors. *Coord. Chem. Rev.* **2016**, *307*, 361−381.

(12) Ouyang, J.; He, Z.; Zhang, Y.; Yang, H.; Zhao, Q. Trimetallic FeCoNi@C Nanocomposite Hollow Spheres Derived from Metal-Organic Frameworks with Superior Electromagnetic Wave Absorption Ability. *ACS Appl. Mater. Interfaces* **2019**, *11*, 39304−39314.

(13) Yan, L.; Cao, L.; Dai, P.; Gu, X.; Liu, D.; Li, L.; Wang, Y.; Zhao, X. Metal-Organic Frameworks Derived Nanotube of Nickel-Cobalt Bimetal Phosphides as Highly Efficient Electrocatalysts for Overall Water Splitting. *Adv. Funct. Mater.* **2017**, *27*, No. 1703455.

(14) Tranchemontagne, D. J.; Hunt, J. R.; Yaghi, O. M. Room temperature synthesis of metal-organic frameworks: MOF-5, MOF-74, MOF-177, MOF-199, and IRMOF-0. *Tetrahedron* **2008**, *64*, 8553−8557.

(15) (a) Salunkhe, R. R.; Kaneti, Y. V.; Yamauchi, Y. Metal-Organic Framework-Derived Nanoporous Metal Oxides toward Supercapacitor Applications: Progress and Prospects. *ACS Nano* **2017**, *11*, 5293−5308. (b) Liu, X. B.; Li, W. X.; Zhao, X. D.; Liu, Y. C.; Nan, C. W.; Fan, L. Z. Two Birds with One Stone: Metal-Organic Framework Derived Micro-/Nanostructured Ni_2P/Ni Hybrids Embedded in Porous Carbon for Electrocatalysis and Energy Storage. *Adv. Funct. Mater.* **2019**, *29*, No. 1901510.

(16) Jung, B. Y.; Lim, H. S.; Sun, Y. K.; Suh, K. D. Synthesis of Fe_3O_4/C composite microspheres for a high performance lithium-ion battery anode. *J. Power Sources* **2013**, *244*, 177−182.

(17) Zhu, B.; Liu, Y.; Zhao, H.; Zhang, X.; He, P.; Wu, L.; Liu, Y.; Yang, T. ZnOHF/N-doped carbon hybrids as a novel anode material for enhanced lithium storage. *J. Alloys Compd.* **2022**, *889*, No. 161705.

(18) Zhao, H.; He, P.; Liu, Y.-G.; Zhu, B.; Zhang, X.; Mi, R. 3D pomegranate-like structured Si@void@Ni@C microspheres as high-performance anode in lithium-ion batteries. *Appl. Phys. Lett.* **2021**, *119*, No. 083903.

(19) Zhang, X.; He, P.; Dong, B.; Mu, N.; Liu, Y.; Yang, T.; Mi, R. Synthesis and characterization of metal-organic framework/biomass-derived CoSe/C@C hierarchical structures with excellent sodium storage performance. *Nanoscale* **2021**, *13*, 4167−4176.

(20) (a) Li, X. G.; Takahashi, S. Synthesis and magnetic properties of Fe-Co-Ni nanoparticles by hydrogen plasma-metal reaction. *J. Magn. Magn. Mater.* **2000**, *214*, 195−203. (b) Kim, T.; Lee, J.; Lee, K.; Park, B.; Jung, B. M.; Lee, S. B. Magnetic and dispersible FeCoNi-

graphene film produced without heat treatment for electromagnetic wave absorption. *Chem. Eng. J.* **2019**, *361*, 1182−1189.
(21) Bulut Kopuklu, B.; Tasdemir, A.; Alkan Gursel, S.; Yurum, A. High stability graphene oxide aerogel supported ultrafine Fe_3O_4 particles with superior performance as a Li-ion battery anode. *Carbon* **2021**, *174*, 158−172.
(22) Yang, Z.; Su, D. Y.; Yang, J. P.; Wang, J. Fe3O4/C composite with hollow spheres in porous 3D-nanostructure as anode material for the lithium-ion batteries. *J. Power Sources* **2017**, *363*, 161−167.
(23) Hao, S.; Zhang, B.; Wang, Y.; Li, C.; Feng, J.; Ball, S.; Srinivasan, M.; Wu, J.; Huang, Y. Hierarchical three-dimensional Fe_3O_4@porous carbon matrix/graphene anodes for high performance lithium ion batteries. *Electrochim. Acta* **2018**, *260*, 965−973.
(24) (a) Li, X. N.; Rykov, A. I.; Zhang, B.; Zhangc, Y. J.; Wang, J. H. Graphene encapsulated Fe_xCo_y nanocages derived from metal-organic frameworks as efficient activators for peroxymonosulfate. *Catal. Sci. Technol.* **2016**, *6*, 7486−7494. (b) Sun, G. B.; Wu, H.; Liao, Q. L.; Zhang, Y. Enhanced microwave absorption performance of highly dispersed CoNi nanostructures arrayed on graphene. *Nano Res.* **2018**, *11*, 2689−2704.
(25) Wang, X. L.; Xiao, H.; Li, A.; Li, Z.; Liu, S. J.; Zhang, Q. H.; Gong, Y.; Zheng, L. R.; Zhu, Y. Q.; Chen, C.; et al. Constructing $NiCo/Fe_3O_4$ Heteroparticles within MOF-74 for Efficient Oxygen Evolution Reactions. *J. Am. Chem. Soc.* **2018**, *140*, 15336−15341.
(26) Bates, M. K.; Jia, Q.; Doan, H.; Liang, W.; Mukerjee, S. Charge-Transfer Effects in Ni-Fe and Ni-Fe-Co Mixed-Metal Oxides for the Alkaline Oxygen Evolution Reaction. *ACS Catal.* **2016**, *6*, 155−161.
(27) Zhang, X. T.; Yuan, Y. F.; Zhu, M.; Cai, G. C.; Tong, Z. W.; Yang, Z. Y. 3D porous framework of ZnO nanoparticles assembled from double carbon shells consisting of hard and soft carbon networks for high performance lithium ion batteries. *Nanotechnology* **2020**, *31*, No. 285402.
(28) Zhang, Q. M.; Shi, Z. C.; Deng, Y. F.; Zheng, J.; Liu, G. C.; Chen, G. H. Hollow Fe_3O_4/C spheres as superior lithium storage materials. *J. Power Sources* **2012**, *197*, 305−309.
(29) Yu, M.; Sun, L. Y.; Ning, X. H. Controllable synthesis of carbon-coated Fe_3O_4 nanorings with high Li/Na storage performance. *J. Alloys Compd.* **2021**, *878*, No. 160359.
(30) Jin, S.; Deng, H.; Long, D.; Liu, X.; Zhan, L.; Liang, X.; Qiao, W.; Ling, L. Facile synthesis of hierarchically structured Fe_3O_4/carbon micro-flowers and their application to lithium-ion battery anodes. *J. Power Sources* **2011**, *196*, 3887−3893.
(31) (a) Wu, S. H.; Han, Y. D.; Wen, K. C.; Wei, Z. H.; Chen, D. J.; Lv, W. Q.; Lei, T. Y.; Xiong, J.; Gu, M.; He, W. D. Composite nanofibers through in-situ reduction with abundant active sites as flexible and stable anode for lithium ion batteries. *Composites, Part B* **2019**, *161*, 369−375. (b) Yang, T.; Yang, D. X.; Liu, Y. G.; Liu, J.; Chen, Y. F.; Bao, L.; Lu, X. X.; Xiong, Q. Q.; Qin, H. Y.; Ji, Z. G.; et al. MOF-derived carbon-encapsulated cobalt sulfides orostachys-like micro/nano-structures as advanced anode material for lithium ion batteries. *Electrochim. Acta* **2018**, *290*, 193−202.
(32) Yang, T.; Zhong, J. S.; Liu, J. W.; Yuan, Y. J.; Yang, D. X.; Mao, Q. N.; Li, X. Y.; Guo, Z. P. A General Strategy for Antimony-Based Alloy Nanocomposite Embedded in Swiss-Cheese-Like Nitrogen-Doped Porous Carbon for Energy Storage. *Adv. Funct. Mater.* **2021**, *31*, No. 2009433.

https://doi.org/10.1021/acsomega.2c01988
ACS Omega 2022, 7, 16837−16846